

Zero-Shot Detection of Elastic Transient Morphology Across Physical Systems

Jose Sánchez Andreu¹

¹Independent Researcher, Murcia, Spain

(Dated: January 19, 2026)

We test whether a representation learned from interferometric strain transients in gravitational-wave observatories can act as a frozen morphology-sensitive operator for unseen sensors, provided the target signals preserve coherent elastic transient structure. Using a neural encoder trained exclusively on non-Gaussian instrumental glitches, we perform strict zero-shot anomaly analysis on rolling-element bearings without retraining, fine-tuning, or target-domain labels.

On the IMS–NASA run-to-failure dataset, the operator yields a monotonic health index $HI(t) = s_{0.99}(t)/\tau$ normalized to an early-life reference distribution, enabling fixed false-alarm monitoring at $1 - q = 10^{-3}$ with $\tau = Q_{0.999}(\mathcal{P}_0)$. In discrete fault regimes (CWRU), it achieves strong window-level discrimination ($AUC_{\text{win}} \approx 0.90$) and file-level separability approaching unity ($AUC_{\text{file}} \approx 0.99$). Electrically dominated vibration signals (VSB) show weak, non-selective behavior, delineating a physical boundary for transfer.

Under a matched IMS controlled-split protocol, a generic EfficientNet-B0 encoder pretrained on ImageNet collapses in the intermittent regime ($\Lambda_{\text{tail}} \approx 2$), while the interferometric operator retains strong extreme-event selectivity ($\Lambda_{\text{tail}} \approx 860$), indicating that the effect is not a generic property of CNN features. Controlled morphology-destruction transformations selectively degrade performance despite per-window normalization, consistent with sensitivity to coherent time–frequency organization rather than marginal amplitude statistics.

I. INTRODUCTION

The detection and characterization of transient phenomena is central across experimental physics. Short-duration deviations from nominal behavior often signal nonlinear dynamics, changes in boundary conditions, or localized dissipation not captured by stationary or time-averaged descriptions. In precision interferometry, weak non-Gaussian strain transients must be identified and mitigated to ensure reliable scientific inference; in rotating mechanical systems, transient elastic responses driven by impacts, frictional contacts, and incipient defects are primary indicators of structural degradation and instability.

Despite vast differences in physical scale and sensing modality, both settings share a common mechanism: elastic wave propagation in constrained media. Material properties, geometric confinement, and boundary conditions jointly govern dispersion, reflection, and the temporal organization of propagating wave packets, so elastic transients are structured objects whose time–frequency organization reflects the physics of the medium. In interferometric detectors, such disturbances arise from suspension friction, scattered light, seismic upconversion, and opto-mechanical instabilities; in rolling-element bearings, analogous responses emerge from localized contact mechanics, surface defects, and impulsive load transfer across raceways. While characteristic frequencies, amplitudes, and units differ by orders of magnitude, both classes of systems impose strong physical constraints that can organize transient energy coherently across time and frequency. This motivates the hypothesis that certain *coherently organized time–frequency morphologies* of non-Gaussian elastic transients may be preserved across physically distinct systems when propagation remains elastic

and constrained.

In gravitational-wave interferometers, non-Gaussian strain transients (“glitches”) are a major detector-characterization challenge [1–3]. Prior work has shown that glitch populations exhibit rich, repeatable time–frequency morphologies that can be learned from data and exploited for monitoring and data-quality assessment. Yet most transient-detection approaches remain strongly domain-specific: gravitational-wave pipelines rely on detailed instrument models, transfer functions, and heuristics, while mechanical condition monitoring typically trains detectors on the target machinery, requiring labels, retraining, or domain adaptation as operating conditions change. Both paradigms tend to couple detection to absolute frequency content, signal energy, or stationary descriptors, and can therefore miss nonstationary transient structure governed by elastic propagation rather than static spectral content.

Here we test a different hypothesis: that a representation trained to encode the *morphological structure* of elastic transients can function as a fixed physical operator across domains, independent of absolute scale and sensor modality. We study a latent operator \mathcal{F} trained exclusively on interferometric strain transients and evaluate whether it exhibits selective anomaly sensitivity when applied *zero-shot* to rotating mechanical systems. Rather than acting as a domain-specific classifier, \mathcal{F} operates as a morphology-sensitive projection from normalized time–frequency representations into a latent space that encodes structural regularities associated with elastic wave propagation.

This view is summarized schematically in Fig. 1 by treating the trained representation as a fixed measurement operator acting on normalized time–frequency structure.

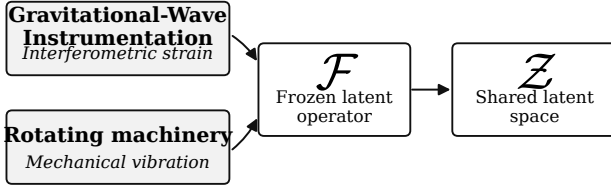


FIG. 1. Conceptual framework for cross-domain morphological analysis. A fixed latent operator \mathcal{F} , trained exclusively on interferometric strain transients (source domain), maps normalized time–frequency representations from multiple physical systems into a shared latent space \mathcal{Z} . The operator acts as a morphology-sensitive projection that suppresses dependence on absolute scale and sensor modality, while preserving structural organization associated with elastic wave propagation in constrained media. Zero-shot anomaly sensitivity emerges only when target-domain signals preserve compatible elastic transient structure; systems lacking mechanically mediated propagation do not exhibit separation.

We evaluate this hypothesis in both discrete fault regimes and progressive degradation. Using the IMS-NASA run-to-failure bearing dataset, we test whether the fixed operator \mathcal{F} captures monotonic drift, yields an interpretable health indicator, and enables early deviation detection under a controlled false-alarm rate, without retraining or access to fault-domain labels. We also evaluate separability on the CWRU bearing dataset under controlled fault conditions, and use electrically dominated vibration signals as a negative control to delineate the physical boundary of transfer. Classical treatments of elastic and acoustic wave propagation in solids emphasize that transient structure is governed primarily by material properties, geometry, and boundary conditions rather than absolute scale [4, 5].

To ensure falsifiability, we treat \mathcal{F} as a fixed measurement device and probe its response under controlled morphology-destruction transformations (e.g., spectral filtering, temporal smearing, and reverberation-induced self-interference). These interventions preserve marginal amplitude statistics through per-window normalization while selectively disrupting time–frequency organization. If sensitivity were driven by generic distributional shifts or energy cues, performance would be invariant; transformation-dependent degradation instead implicates preserved time–frequency structure rather than amplitude-based or stationary statistical effects.

We emphasize that the reported invariance is empirical and representation-induced, not a fundamental symmetry of the governing equations: \mathcal{F} does not encode a conserved quantity, but acts as a fixed instrument whose response reveals shared structural regularities under the stated protocol. Likewise, “zero-shot” refers here to an *experimental deployment protocol*: \mathcal{F} encodes a prior learned solely from *source-domain* interferometric transient physics and is then held frozen; no target-domain samples, labels, hyperparameter tuning, calibration, or

adaptation are used to shape the representation or the decision rule.

The remainder of this paper is organized as follows. Section II describes the physical systems, datasets, and experimental protocol. Section III presents the run-to-failure analysis, zero-shot transfer, and controlled degradation experiments. Section IV discusses the physical interpretation and limitations, followed by concluding remarks in Sec. V.

II. EXPERIMENTAL SETUP AND METHODS

A. Physical Systems and Datasets

The experiments reported in this work are designed to probe whether a fixed latent representation, trained on interferometric strain transients, exhibits selective sensitivity to elastic transient morphology across physically unrelated systems. We therefore consider signals arising in constrained solid media that span disparate spatial scales, sensing modalities, and operating regimes, but share a common physical mechanism: elastic wave generation and propagation governed by material properties, geometric confinement, and boundary conditions.

By construction, all datasets are treated as passive measurement records. No system-specific modeling, retraining, or domain adaptation is performed in the target domains. The latent operator \mathcal{F} is trained once on a single source domain and subsequently applied as a fixed measurement device under a strict zero-shot protocol. Details on source-domain training, preprocessing, and statistical scoring are provided in the Supplemental Material.

a. Source domain: Interferometric strain transients. The source domain consists of interferometric strain time series $h(t) = \Delta L/L$ acquired from gravitational-wave detector instrumentation. These data contain short-duration, non-Gaussian transients (instrumental glitches) arising from suspension friction, seismic coupling, scattered light, and opto-mechanical instabilities within complex optical assemblies. The measured signals are broadband, nonstationary, and shaped by elastic wave propagation through suspended and mechanically coupled components.

A dataset comprising $\mathcal{O}(10^5)$ labeled transient events recorded during nominal detector operation is used exclusively to train the latent operator \mathcal{F} . No information from any mechanical target domain is used during training. After training, \mathcal{F} is frozen and applied without modification in all subsequent experiments.

b. Target domain A: Run-to-failure degradation (IMS-NASA). The primary target domain is the IMS-NASA run-to-failure bearing dataset, which records the full temporal evolution of rolling-element bearings from nominal operation to catastrophic failure. Vibration signals are acquired via accelerometers mounted on a rotating mechanical test rig, providing a physically grounded

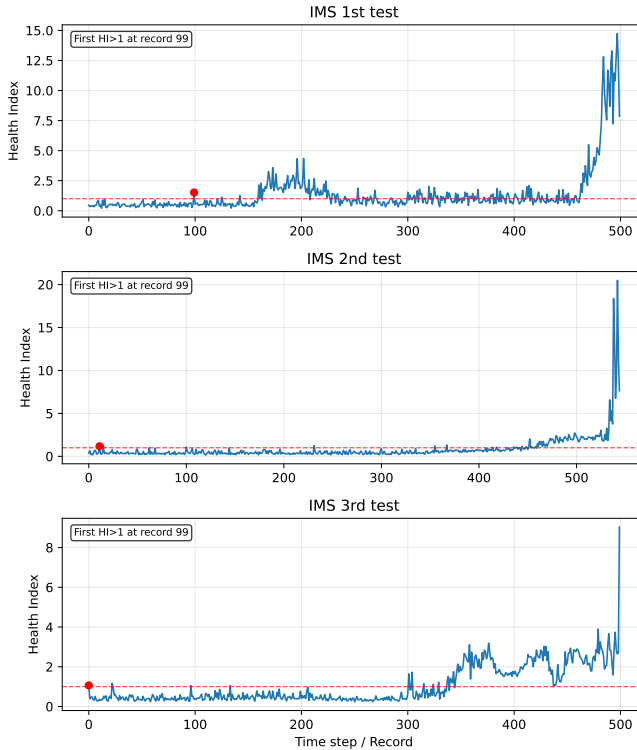


FIG. 2. **Zero-shot run-to-failure monitoring on IMS-NASA.** Health Index trajectories for the three IMS bearing run-to-failure experiments, computed under a strict zero-shot protocol using a frozen operator trained on interferometric strain transients. The horizontal axis denotes record index (chronological order). For each record, window-level scores are aggregated via the $q = 0.99$ quantile and normalized by a fixed nominal threshold τ , defined as the $q = 0.999$ quantile of the early-life reference distribution \mathcal{P}_0 , corresponding to a nominal false-alarm probability of 10^{-3} . The red dashed line marks $HI = 1$ (nominal tail threshold) and the red marker indicates the first threshold crossing.

record of progressive mechanical degradation driven by localized contact mechanics and elastic wave propagation. Figure 2 summarizes the resulting Health Index trajectories for the three IMS run-to-failure experiments under the fixed false-alarm protocol. Unlike static fault benchmarks, this dataset enables the analysis of temporal phenomena, including monotonic drift, early deviation from nominal behavior, and the evolution of a continuous Health Index. We analyze three independent run-to-failure trajectories (1st, 2nd, and 3rd tests), each exhibiting distinct degradation dynamics. This dataset constitutes the central experimental evidence for evaluating whether a fixed morphological operator can track physical aging and incipient failure without retraining or access to fault labels.

c. Target domain B: Discrete fault regimes (CWRU). As a complementary regime, we consider the Case Western Reserve University (CWRU) bearing dataset, which provides vibration recordings under controlled fault and

no-fault conditions at steady operating points. The dataset is provided by the CWRU Bearing Data Center [6]. Unlike IMS, CWRU does not capture temporal degradation, but instead offers clean separation between nominal and faulty mechanical states.

Rolling-element bearing diagnostics and condition monitoring have a long history in vibration analysis, where fault-induced elastic impacts excite guided waves in raceways, rolling elements, and housings. Early work established the importance of high-frequency resonance and impulsive response for bearing fault detection [7]. More recent benchmarks have formalized standard datasets and evaluation protocols for vibration-based diagnostics [8, 9].

Performance on CWRU is reported at two resolutions: window-level (AUC_{win}) and file-level aggregation (AUC_{file}).

d. Negative control: Electrically dominated vibration (VSB). To delineate the physical domain of validity, we evaluate the same frozen operator on the VSB power-line fault dataset, whose signals are dominated by narrow-band electromagnetic interference and incoherent sensor noise rather than mechanically mediated elastic-wave propagation [10]. If the reported transfer were driven by generic non-Gaussianity or distributional shift, comparable separation would be expected in this regime; instead, VSB serves as a negative control for physically specific elastic-transient morphology.

All datasets are processed using the identical time-frequency pipeline described in Sec. II B, enabling a strict zero-shot evaluation.

In the IMS run-to-failure dataset, each measurement file acquired at a given time is treated as a *record*. Each record is segmented into overlapping windows, scored at the window level, and aggregated into record-level statistics (e.g., upper quantiles) to produce a time-resolved Health Index $HI(t)$.

All datasets use the fixed preprocessing pipeline in Sec. II B.

TABLE I. Signal processing parameters defining the time-frequency resolution. The target sampling rate is chosen to align the elastic transient scale with the receptive field of the interferometric operator.

Parameter	Symbol	Value	Unit
Target sampling rate	f_s	4096	Hz
Window size	N_{win}	256	samples
Hop length	N_{hop}	128	samples
FFT points	N_{fft}	256	bins
Temporal resolution	Δt	31.25	ms
Spectral resolution	Δf	16.0	Hz
Receptive field	T_{RF}	≈ 1.5	s

B. Time–Frequency Representation and Preprocessing

All signals are projected onto a fixed time–frequency representation prior to embedding. The latent operator \mathcal{F} operates exclusively on pre-generated spectrograms and does not access time-domain waveforms directly; consequently, all time–frequency parameters are defined as part of the preprocessing protocol and are held fixed across domains. Signals are resampled to a common $f_s = 4096$ Hz to fix a shared time–frequency grid and to match the transient time scale to the encoder’s effective receptive field. The value is a convenient power-of-two choice for consistent STFT windowing; stronger downsampling erases short elastic transients. We compute Hann STFT spectrograms using $N_{\text{win}} = 256$, $N_{\text{hop}} = 128$, and $N_{\text{ftt}} = 256$, yielding $\Delta f = 16$ Hz and $\Delta t = 31.25$ ms, sufficient to resolve short elastic transients at the chosen grid.

All spectrograms are log-amplitude scaled and standardized independently on a per-window basis. This normalization removes explicit dependence on absolute signal amplitude, physical units, and sensor modality while preserving the relative organization of energy across time and frequency. As a result, the operator responds to dimensionless morphological structure rather than to scale-dependent or stationary statistical features.

C. Latent Morphological Operator and Anomaly Scoring

Inputs to the frozen encoder are standardized log-amplitude spectrogram windows constructed with a fixed preprocessing pipeline (Sec. II B). Per-window standardization suppresses absolute scale while preserving relative time–frequency organization. We emphasize that although the operator \mathcal{F} is trained on a source domain, it is not adapted, re-optimized, or re-calibrated in any way for the target domains. All target-domain results therefore arise from the fixed geometry of the latent space induced during source-domain training. Throughout, \mathcal{F} is treated as a fixed measurement instrument: after source-domain training, the encoder is frozen and used only to induce a geometry on normalized time–frequency inputs. The downstream anomaly score and threshold are defined independently from this geometry using nominal target-domain reference data, without any optimization against abnormal conditions.

a. Latent morphological operator. The latent operator \mathcal{F} acts as a fixed measurement map from normalized time–frequency structure to a latent representation,

$$\mathcal{F} : X \in \mathbb{R}^{M \times N} \mapsto z \in \mathcal{Z} \subset \mathbb{R}^d, \quad (1)$$

z empirically reflects structural regularities associated with elastic transient organization. In this work, \mathcal{F} is a convolutional encoder that produces a pooled $d = 1280$

embedding. The classifier head used during source-domain training is discarded, and the encoder is frozen for all target-domain experiments.

b. Score convention. Throughout this work we report the *distance-form* Mahalanobis score

$$\mathcal{S}(z) = \sqrt{(z - \mu_0)^\top \Sigma_{\text{LW}}^{-1} (z - \mu_0)}. \quad (2)$$

All quantiles, detection thresholds, tail statistics, and Health Index definitions are computed consistently on \mathcal{S} in Eq. (2). The corresponding quadratic form $\mathcal{S}^2(z)$ is related by $\mathcal{S}(z) = \sqrt{\mathcal{S}^2(z)}$ and is not used elsewhere for thresholding, aggregation, or reporting.

c. Aggregation levels and AUC metrics. We report performance at three complementary aggregation levels. At the window level, AUC_{win} evaluates instantaneous discrimination between nominal and faulty windows. At the file level, AUC_{file} is computed by aggregating window scores within each signal file using the arithmetic mean, reflecting diagnostic separability when labels are associated with entire recordings. For run-to-failure experiments, we report a record-level metric AUC_{rec} , where each temporal record is summarized by a high quantile ($q = 0.95$ or 0.99) of its window scores, enabling early detection under a fixed false-alarm threshold.

d. Anomaly scoring. Deviations from nominal behavior are quantified relative to a reference distribution \mathcal{P}_0 constructed from embeddings associated with an operational early-life period in the target domain. Given the high dimensionality of the embedding space ($d = 1280$) and the finite sample size of the reference set, standard covariance estimation is ill-conditioned. More broadly, anomaly detection aims to identify deviations from nominal behavior without explicit supervision on abnormal classes. Comprehensive surveys have highlighted the diversity of statistical, distance-based, and learning-based approaches to this problem [11]. In high-dimensional settings, distance-based detectors in learned embedding spaces have emerged as a practical compromise between interpretability and expressivity [12]. We therefore employ the Ledoit–Wolf shrinkage estimator [13] to obtain a well-conditioned covariance matrix Σ_{LW} and compute anomaly scores using Eq. (2). We use the distance-form Mahalanobis score so that all thresholds and tail statistics are defined on a consistent scale.

D. Run-to-Failure Analysis: Drift, Time-to-Detection, and Health Index

To assess whether the latent operator \mathcal{F} captures physically meaningful degradation dynamics rather than static state separation, we apply it to the IMS–NASA run-to-failure bearing dataset. Unlike discrete fault benchmarks, this dataset provides a continuous temporal record from nominal operation to catastrophic failure, enabling direct analysis of progressive damage accumulation, early deviation, and long-term drift under realistic operating conditions. The IMS–NASA run-to-failure

dataset provides full-life vibration recordings of rolling-element bearings from nominal operation to catastrophic failure and is widely used for studying degradation dynamics and prognostics. The dataset was originally released through the NASA Ames Prognostics Data Repository [14].

a. Baseline definition. A nominal reference distribution \mathcal{P}_0 is constructed from the first N records of each run, corresponding to early-life operation. Unless stated otherwise, we use $N = 100$; for IMS 2nd_test, where an extended steady-state segment is present, we use $N = 200$. No data from later stages of the run are used to define the baseline or detection thresholds.

b. Health Index. To obtain a time-resolved measure of system condition, window-level anomaly scores are aggregated at the record level using upper quantiles of their empirical distribution. For a record acquired at time t , we define the dimensionless Health Index

$$HI(t) = \frac{s_q(t)}{\tau}, \quad (3)$$

where $s_q(t)$ is the q -th quantile of the window-level anomaly scores within the record ($q = 0.99$ unless otherwise specified), and τ is the fixed detection threshold derived from the nominal reference distribution \mathcal{P}_0 .

By construction, $HI(t) = 1$ corresponds to the extreme tail of nominal operation under the chosen false-alarm convention, while $HI(t) > 1$ indicates excess occupancy of structurally anomalous transient events. This definition suppresses sensitivity to shifts in central tendency and instead emphasizes the emergence and persistence of rare, high-severity deviations in latent space, consistent with extreme-event detection paradigms in experimental physics.

Normalization by τ renders the Health Index dimensionless and directly comparable across runs, independent of absolute score scale or operating conditions.

c. Time-to-Detection (TTD). We define the Time-to-Detection (TTD) as the earliest record at which the Health Index persistently exceeds unity,

$$TTD = \min \{t : HI(t) > 1 \text{ for at least } K \text{ consecutive records}\} \quad (4)$$

with $K = 3$ unless otherwise stated. This persistence criterion suppresses spurious threshold crossings due to isolated fluctuations and identifies the earliest statistically significant deviation from the nominal elastic transient morphology under a fixed false-alarm rate.

TTD is computed without access to failure labels, trend fitting, or domain-specific thresholds, and therefore constitutes an unsupervised early warning indicator derived entirely from the fixed operator response.

d. Drift analysis. To determine whether the temporal evolution of the Health Index reflects systematic degradation rather than stochastic variability, we quantify monotonic drift using Spearman's rank correlation coefficient ρ between $HI(t)$ and record index. Spearman correlation is chosen to capture monotonic trends with-

out assuming linearity or a specific functional form for the degradation trajectory.

A statistically significant positive ρ indicates ordered progression of elastic transient morphology over the component lifetime. Across all IMS runs, we observe strong positive correlations with extremely small p -values, confirming that the latent operator captures time-ordered structural evolution rather than isolated outliers or random excursions.

e. Interpretation. Both the Health Index and the Time-to-Detection are derived entirely from a frozen operator trained on interferometric strain transients, without retraining, calibration, or adaptation to the IMS dataset. Consequently, any temporal structure observed in $HI(t)$ reflects alignment between the evolving elastic transient morphology of the mechanical system and the structural regularities encoded by \mathcal{F} , rather than supervised learning, explicit modeling of bearing dynamics, or retrospective optimization.

This protocol enables a direct and falsifiable evaluation of zero-shot degradation tracking and early deviation detection in a physically aging system, forming the central experimental test of cross-domain morphological sensitivity in this work.

E. IMS Controlled-Split Protocol for Encoder Comparisons

The IMS run-to-failure experiments in Sec. II D use the full trajectories to quantify drift, early deviation, and health-index evolution. In addition, we introduce a controlled-split evaluation protocol designed specifically to (i) enable matched comparisons between different frozen encoders and (ii) isolate regimes where degradation manifests as intermittent elastic impacts rather than as global spectral drift.

For each selected IMS trajectory, we construct three disjoint record sets: (i) a nominal reference set \mathcal{P}_0 drawn from the early-life segment, (ii) a held-out nominal test segment, and (iii) a late-life abnormal segment. In all experiments reported in Sec. III C, we use $N_0 = 120$ records for \mathcal{P}_0 , and evaluate on $N_{\text{nom}} = 250$ held-out nominal records and $N_{\text{abn}} = 250$ late-life records, yielding 620 records per trajectory. No records from the test segments are used to estimate μ_0 , Σ_{LW} , or the threshold τ .

All records are processed using the identical STFT and per-window standardization pipeline described in Sec. II B. Window-level anomaly scores are computed using the Mahalanobis distance in latent space (Sec. II C) and aggregated to record-level statistics using the $q = 0.95$ quantile, denoted $s_{0.95}(t)$. Performance is summarized using (i) window-level discrimination AUC_{win} , (ii) record-level discrimination AUC_{rec} computed from $s_{0.95}(t)$, and (iii) tail enrichment Λ_{tail} under the fixed nominal threshold $\tau = Q_{0.999}(\mathcal{P}_0)$.

a. Matched generic baseline (ImageNet). To test whether the observed cross-domain sensitivity is specific to the interferometric morphological prior, we repeat the entire controlled-split protocol using a frozen EfficientNet-B0 encoder pre-trained on ImageNet. This baseline shares the same architecture, embedding dimensionality ($d = 1280$), preprocessing, anomaly scoring, thresholding, and aggregation. The only difference is the source of the frozen representation: (i) interferometric strain transients (morphological operator \mathcal{F}) versus (ii) natural-image supervision (generic baseline).

b. Physical descriptors (RMS and kurtosis). To probe the physical observable driving separation in the intermittent regime, we compute classical record-level descriptors on the raw time series (channel 0): Root Mean Square (RMS) as a proxy for signal energy and kurtosis as a proxy for impulsivity. We report correlations between these descriptors and the record-level anomaly statistic $s_{0.95}$ for both encoders.

F. Statistical Thresholding and Tail Enrichment

Anomalous behavior is characterized relative to a fixed nominal reference distribution \mathcal{P}_0 , constructed exclusively from early-life or known-normal data and held fixed throughout all experiments. No information from abnormal conditions enters the estimation of thresholds or scores at any stage, ensuring a strictly one-sided and physically interpretable protocol.

Rather than posing anomaly detection as a binary classification problem, we adopt a tail-based characterization aligned with rare-event analyses in experimental physics, where meaningful deviations appear as excess occupancy in the extreme tails of a background distribution rather than as shifts in central tendency. No sequential change-detection schemes (e.g., CUSUM, SPRT, or EWMA) are required: all results are derived solely from fixed-window anomaly scores, record-level aggregation, and quantile-based thresholds defined *a priori* from \mathcal{P}_0 . Accordingly, Λ_{tail} is interpreted as a descriptive effect-size measure under a fixed nominal false-alarm convention, not as a discovery statistic or a claim of universality.

a. Quantile-based thresholding. A detection threshold is defined as a high quantile of the nominal score distribution,

$$\tau = Q_q(\mathcal{P}_0), \quad (5)$$

with $q = 0.999$ unless otherwise stated, corresponding to a nominal false-alarm probability $1 - q = 10^{-3}$. The threshold is estimated once from \mathcal{P}_0 and applied uniformly across all datasets, runs, and experimental conditions. Finite-sample variability of τ is negligible compared to the dynamic range observed under abnormal conditions, and the results are stable under moderate variations of q .

b. Tail enrichment. Given the fixed threshold τ , we define the tail enrichment factor

$$\Lambda_{\text{tail}} = \frac{\mathbb{P}(\mathcal{S}(z) > \tau \mid \text{abnormal})}{\mathbb{P}(\mathcal{S}(z) > \tau \mid \text{nominal})}. \quad (6)$$

By construction, the denominator equals $1 - q$, providing a normalized and physically interpretable baseline. Values $\Lambda_{\text{tail}} \gg 1$ indicate strong excess occupancy of extreme latent events relative to nominal operation, while $\Lambda_{\text{tail}} \approx 1$ indicates no measurable enrichment beyond statistical expectation. This formulation emphasizes changes in extreme-event occupancy and is insensitive to shifts in mean score or bulk statistics.

c. Robustness and physical selectivity. Tail enrichment remains stable across high-quantile choices $q \in [0.995, 0.9995]$, with Λ_{tail} varying by less than a factor of two. In contrast, negative-control conditions—including electrically dominated signals and controlled morphology-destruction transformations—yield $\Lambda_{\text{tail}} \approx 1$ independently of threshold choice.

As shown in Sec. III, rotating mechanical systems under fault or advanced degradation exhibit pronounced enrichment ($\Lambda_{\text{tail}} \sim 10^1\text{--}10^2$), whereas systems lacking coherent elastic wave propagation do not. This contrast demonstrates that extreme-score enrichment arises only when structured time-frequency organization associated with elastic transients is preserved. Accordingly, Λ_{tail} quantifies the response of the fixed operator \mathcal{F} to preserved elastic transient morphology, rather than serving as a hypothesis-test statistic.

G. Controlled Morphological Degradation

To determine whether the observed cross-domain anomaly sensitivity reflects a physically meaningful structural effect rather than a statistical artefact, we introduce a controlled degradation protocol that selectively disrupts the *morphological organization* of elastic transients. The central objective is to progressively destroy coherent time-frequency structure while preserving, up to per-window normalization, low-order amplitude statistics.

If anomaly sensitivity were driven by generic distributional mismatch, signal energy, or variance-based cues, detection performance would remain largely invariant under such transformations. Conversely, if sensitivity is governed by structured elastic transient morphology, performance should degrade in a selective and transformation-dependent manner. The protocol therefore constitutes a direct falsification test of the physical hypothesis underlying the reported zero-shot transfer.

a. Design principle. All transformations are constructed such that, after per-window normalization, first- and second-order amplitude moments are conserved. As a result, trivial cues related to signal power, variance, or stationary spectral content are suppressed. Any systematic loss of anomaly sensitivity must therefore arise

from disruption of coherent time–frequency organization rather than from changes in marginal statistics.

b. Transformation families. We consider three classes of morphology-altering transformations, each applied in the time domain prior to time–frequency projection:

1. *Spectral low-pass filtering*, which progressively removes high-frequency components while preserving integrated signal energy.
2. *Temporal smearing*, implemented via convolution with a finite-width kernel, degrading time localization without altering total spectral power.
3. *Reverberation-induced self-interference*, implemented through multi-tap delay lines that introduce phase dispersion and temporal incoherence while preserving spectral support.

All transformed signals are subsequently standardized on a per-window basis, ensuring matched mean and variance relative to the corresponding untransformed windows.

c. Degradation levels. For each transformation family, three degradation levels are defined: a control condition (L_0) with no additional morphological perturbation beyond the intrinsic processing pipeline; a moderate degradation level (L_1), corresponding to partial disruption of transient coherence; and a strong degradation level (L_2), designed to effectively destroy coherent time–frequency organization through aggressive filtering, smearing, or phase-dispersive interference.

d. Falsifiable prediction. If anomaly sensitivity is governed by elastic transient morphology, detection performance should degrade selectively under transformations that disrupt coherent time–frequency organization, with distinct responses across transformation families and degradation levels. In contrast, invariance of performance across all transformations would falsify the physical interpretation and indicate sensitivity to generic statistical cues. The results reported in Sec. III directly test this prediction.

III. RESULTS

A. Run-to-Failure Degradation and Early Warning (IMS–NASA)

We first evaluate the frozen latent operator \mathcal{F} on the IMS–NASA run-to-failure bearing dataset, which captures the full temporal evolution of mechanical degradation from nominal operation to catastrophic failure. Unlike static fault-classification benchmarks, this regime probes whether the operator can track *progressive physical degradation*, identify early deviation from nominal behavior, and yield an interpretable health indicator under a strict zero-shot protocol.

Across all runs, anomaly scores are computed relative to a fixed nominal baseline \mathcal{P}_0 derived from the early-life segment of each trajectory. A detection threshold τ is defined as the $q = 0.999$ quantile of the nominal distribution, fixing the false-alarm probability *a priori*. Temporal evolution is characterized using the normalized Health Index $HI(t) = s_q(t)/\tau$, hereafter we use $HI(t)$ with $q = 0.99$ unless otherwise stated.

a. Run 1: Noisy progressive degradation. In the first trajectory (IMS 1st_test), classical separability metrics are weak (window-level AUC ≈ 0.55 , record-level AUC ≈ 0.62), indicating that nominal and fault states are not cleanly separable in a static classification sense. Despite this, the operator exhibits a clear and statistically significant monotonic drift in extreme-score statistics. The Health Index increases systematically over time, with a strong positive Spearman correlation ($\rho \approx 0.56$, $p \ll 10^{-40}$).

Early deviation is detected well before final failure: the exceedance rate first surpasses 1% at record index 51, and the normalized Health Index crosses unity at record index 99. The maximum observed severity reaches $HI_{99,\text{max}} \approx 14.7$. This behavior indicates gradual structural degradation rather than a sharp, class-separable transition.

b. Run 2: Clean degradation regime. The second trajectory (IMS 2nd_test) exhibits a markedly cleaner degradation pattern. Nominal and abnormal states occupy well-separated regions of latent space (AUC_{win} ≈ 0.92 , AUC_{rec} ≈ 0.99), but the most salient feature is the exceptionally early emergence of extreme latent events.

The Health Index shows a strong monotonic increase with time ($\rho \approx 0.68$, $p \ll 10^{-70}$) and crosses the nominal threshold at record index 11, long before final failure. Tail enrichment is pronounced ($\Lambda_{\text{tail}} \approx 2.5 \times 10^2$), and the maximum severity reaches $HI_{99,\text{max}} \approx 20.5$, indicating sustained accumulation of extreme morphological deviations without saturation.

c. Run 3: Rapid-onset failure. The third trajectory (IMS 3rd_test) displays a rapid-onset degradation regime. The Health Index remains stable throughout nominal operation before undergoing a sharp transition during the late-life phase. Separability is high (AUC_{win} ≈ 0.90 , AUC_{rec} ≈ 0.98), and extreme-event occupancy increases abruptly, yielding a large tail enrichment ($\Lambda_{\text{tail}} \approx 8.6 \times 10^2$).

The Health Index rapidly exceeds unity and reaches values $HI_{99} \gg 10$, signaling imminent failure with high confidence. This trajectory is consistent with a regime characterized by prolonged stable operation followed by a rapid structural collapse.

d. Interpretation across runs. Across all three trajectories, the latent operator consistently captures monotonic drift in extreme latent events, despite substantial variation in static separability metrics. This demonstrates that window-level or record-level AUC is not the primary indicator of physical sensitivity in run-to-failure settings. Instead, degradation manifests as a progressive

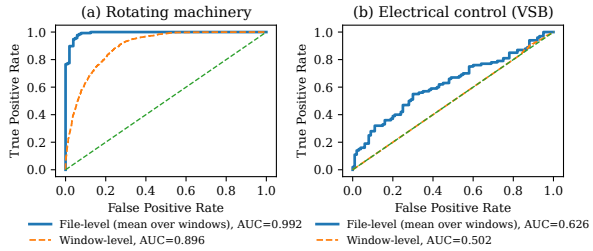


FIG. 3. **Zero-shot performance and physical specificity.** Receiver operating characteristic (ROC) curves for (a) the CWRU rotating machinery dataset (mechanical domain) and (b) the VSB electrical control dataset (electromagnetic domain). Strong discrimination is observed only in mechanically governed systems where elastic transient morphology is preserved, while performance collapses toward chance in electrically dominated signals, establishing a clear physical boundary for zero-shot transfer.

enrichment of rare, structurally anomalous transients.

These results establish the IMS–NASA experiments as the central physical evidence of cross-domain transfer: a representation trained exclusively on interferometric strain transients functions as a zero-shot morphological operator capable of tracking mechanical degradation and providing early warning in a real run-to-failure system.

B. Zero-Shot Transfer in Static Fault Regimes (CWRU and VSB)

Having established that the latent operator \mathcal{F} captures progressive degradation and early deviation in run-to-failure systems (IMS–NASA), we next evaluate its behavior in *static fault regimes*, where mechanical states are discretely labeled but do not evolve continuously in time. This setting serves as a complementary validation of cross-domain transfer, testing whether preserved elastic transient morphology also yields separability under controlled, steady-state fault conditions.

The operator is trained exclusively on interferometric strain transients and is applied without modification in a strict zero-shot setting.

Figure 3(a) reports receiver operating characteristic (ROC) curves for mechanically induced fault conditions in the CWRU bearing dataset. Strong discrimination is observed, with window-level predictions yielding $AUC_{win} \approx 0.90$ and file-level aggregation producing near-perfect separability, $AUC_{file} \approx 0.99$.

The improvement from window-level to file-level discrimination indicates that anomalous morphology is not confined to isolated transient windows, but recurs coherently across multiple realizations within a recording. This persistence is consistent with the behavior observed in the IMS run-to-failure experiments, where degradation manifests as repeated excursions into the extreme tail of the latent distribution rather than as isolated outliers.

As a negative control, the same frozen operator is

applied to electrically dominated vibration signals from the VSB dataset, which are characterized by narrow-band electromagnetic interference and incoherent sensor noise rather than mechanically mediated elastic transients. As shown in Fig. 3(b), discrimination collapses toward chance in this regime, with no measurable tail enrichment ($\Lambda_{tail} \approx 1$ at the nominal false-alarm rate).

The sharp contrast between mechanically governed and electrically dominated systems establishes a clear physical boundary for zero-shot transfer. High anomaly sensitivity emerges only in systems governed by elastic wave propagation in constrained media, while systems lacking such propagation exhibit weak and non-selective responses. This behavior confirms that the latent operator does not respond generically to non-Gaussian statistics, signal energy, or distributional shifts, but instead requires coherent elastic organization to produce separability.

a. Separation across physical scales. For context, source-domain interferometric transients correspond to dimensionless strain amplitudes of order $h \sim 10^{-21}$ at characteristic frequencies of $\mathcal{O}(10^2)$ Hz. In contrast, bearing faults in the CWRU dataset involve localized mechanical impacts producing accelerations of $\mathcal{O}(10^1)$ g at characteristic frequencies of $\mathcal{O}(10^3)$ Hz. The observed zero-shot separability therefore spans radically different sensing modalities, physical units, and characteristic frequency ranges, reinforcing that anomaly sensitivity is not tied to absolute scale or sensor modality, but to preserved organization in elastic transient morphology.

C. Falsification via a Generic Feature Baseline (ImageNet) on IMS

A central question is whether the observed anomaly sensitivity reflects a specific prior for elastic transient morphology learned from interferometric instrumentation, or whether any high-capacity convolutional encoder would produce similar behavior under the same pipeline. To falsify the “generic CNN features” hypothesis, we repeat the IMS analysis under the controlled-split protocol defined in Sec. II E, comparing the interferometric operator with a matched EfficientNet-B0 encoder pre-trained on ImageNet.

Table II summarizes discrimination and extreme-event statistics for the selected IMS trajectories. In the clean degradation regime (2nd_test), both encoders reach high record-level separability, consistent with faults that induce strong global structure. However, in the intermittent regime (IMS 4th_test), where degradation manifests as sparse impacts embedded in a noisy background, the generic baseline collapses: tail enrichment remains near the nominal expectation ($\Lambda_{tail} \approx 2$), while the interferometric operator exhibits massive extreme-event amplification ($\Lambda_{tail} \approx 860$) under the same fixed false-alarm rate.

This dissociation indicates that sensitivity to weak or

TABLE II. IMS controlled-split evaluation (Sec. II E) comparing the frozen interferometric morphological operator and a matched ImageNet-pretrained baseline. Record-level metrics use the $q = 0.95$ score quantile $s_{0.95}$; the tail threshold is fixed as $\tau = Q_{0.999}(\mathcal{P}_0)$.

IMS run	Morphological (LIGO)			Generic (ImageNet)		
	AUC _{win}	AUC _{rec}	Λ_{tail}	AUC _{win}	AUC _{rec}	Λ_{tail}
1st_test	0.616	0.702	1.27	0.543	0.538	1.60
2nd_test	0.999	1.000	191.6	0.921	0.997	19.1
4th_test	0.901	0.982	859.5	0.653	0.652	1.97

TABLE III. Record-level Pearson correlations between the aggregated anomaly statistic $s_{0.95}$ and physical descriptors in the intermittent regime (IMS 4th_test).

Representation	Corr. w/ Kurtosis	Corr. w/ RMS
Morphological (LIGO)	0.7789	0.8998
Generic (ImageNet)	0.6829	0.7520

intermittent elastic anomalies is not a generic property of CNN feature extraction, but depends on the latent geometry induced by training on interferometric non-Gaussian transients.

D. Mechanism: Enhanced Coupling to Impulsivity (Kurtosis) in the Intermittent Regime

To clarify why the interferometric operator outperforms the generic baseline in the intermittent regime, we analyze the coupling between the record-level anomaly statistic $s_{0.95}$ and classical physical descriptors computed on the raw time series: RMS amplitude (proxy for signal energy) and kurtosis (proxy for impulsivity).

Table III reports record-level Pearson correlations for IMS 4th_test under the controlled-split protocol. While both representations correlate with RMS, the interferometric operator exhibits stronger coupling to kurtosis, consistent with higher sensitivity to sparse, impulsive elastic impacts embedded in a noisy background. This enhanced impulsivity coupling explains the divergence in extreme-event statistics: the generic baseline fails to enrich the tail until anomalies alter global texture, whereas the interferometric operator selectively amplifies rare impulsive transients.

E. Controlled Morphological Degradation

To determine whether cross-domain anomaly sensitivity arises from preserved time-frequency organization rather than from marginal statistics or signal energy, we evaluate the frozen operator \mathcal{F} under a set of controlled morphological perturbations. Detection performance is assessed using the protocol defined in Sec. II G,

which selectively disrupts transient structure via (i) spectral low-pass filtering, (ii) temporal smearing, and (iii) reverberation-induced self-interference.

All transformed signals are renormalized on a per-window basis, ensuring that any change in performance cannot be attributed to shifts in first- or second-order amplitude statistics. These transformations are not used for data augmentation or model regularization, but solely as controlled physical interventions designed to probe the operator’s sensitivity to coherent time-frequency organization.

Figure 4 reports the window-level area under the ROC curve (AUC_{win}) as a function of degradation level for each transformation family. While AUC is used here as a convenient summary statistic, the emphasis is on relative trends across transformations rather than on absolute classification performance.

The response of \mathcal{F} depends strongly on the physical nature of the morphological disruption. Spectral low-pass filtering produces a monotonic collapse in anomaly sensitivity as the cutoff frequency is reduced. This trend reflects the progressive removal of high-frequency components that support sharp transient localization, broadband interference, and elastic mode coupling—features central to the morphology encoded in the latent space.

Temporal smearing induces a more moderate degradation. Although transient localization in time is weakened, the global organization of energy across frequency bands remains partially intact, allowing \mathcal{F} to retain a substantial fraction of its discriminative power. This behavior indicates that the operator is not narrowly tuned to impulsive events, but responds to extended, yet coherent, elastic structure.

In contrast, reverberation does not produce a monotonic loss of sensitivity. Under reverberation, the operator maintains $\text{AUC}_{\text{win}} \approx 0.90$ even at strong degradation levels, whereas low-pass filtering reduces AUC_{win} to approximately 0.62. Reverberation redistributes coherent energy across time through delayed self-interference while preserving spectral support, indicating that the operator

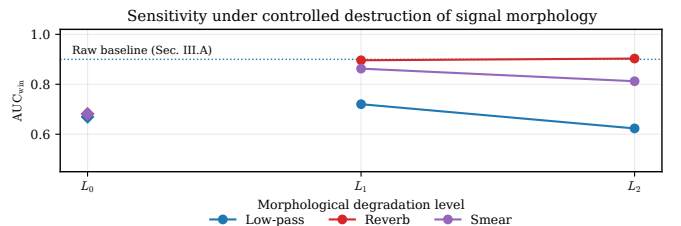


FIG. 4. **Falsification via controlled morphological destruction.** Zero-shot detection performance, quantified by window-level AUC, under transformations that selectively degrade coherent time-frequency structure while preserving marginal amplitude statistics. Selective and transformation-dependent performance degradation indicates sensitivity to elastic transient morphology rather than to signal energy or stationary statistics.

responds to the presence and organization of structured elastic transients rather than to precise temporal alignment or isolated high-amplitude peaks.

Taken together, these perturbation experiments constitute a direct and falsifiable test of the underlying physical hypothesis. If anomaly sensitivity were driven by generic statistical cues, signal energy, or architecture-dependent biases, performance would remain approximately invariant under amplitude-preserving transformations. Instead, separability degrades selectively in a transformation-dependent manner that tracks the preservation or destruction of coherent elastic transient morphology. This behavior supports the interpretation that cross-domain anomaly sensitivity is governed by structured elastic wave phenomena rather than by distributional or energy-based effects.

F. Physical Interpretability and Comparison with Reconstruction-Based Baselines

To assess whether the observed cross-domain anomaly sensitivity reflects physically meaningful structure rather than generic statistical effects, we analyze the anomaly scores produced by the latent operator \mathcal{F} and compare them with those obtained from a reconstruction-based convolutional autoencoder (ConvAE) baseline. The purpose of this comparison is not to rank models by detection performance, but to use each approach as a diagnostic instrument probing which physical observables dominate their respective anomaly responses.

Both operators are evaluated on identical target-domain data under the same preprocessing and scoring pipeline. Their window-level anomaly scores are correlated with a set of classical signal descriptors commonly used in vibration analysis, including amplitude-based measures (e.g., RMS and peak value) and structure-related observables (e.g., effective bandwidth and spectral entropy). Figure 5 reports the resulting Pearson correlation coefficients.

Under the present protocol, ConvAE anomaly scores exhibit non-negligible correlations with amplitude-related descriptors and broader, less selective correlations with higher-order spectral measures. This behavior is consistent with reconstruction error acting as a generic measure of deviation from the training manifold, implicitly coupling sensitivity to a mixture of signal energy, variance, and spectral content.

In contrast, anomaly scores produced by the latent operator \mathcal{F} are nearly orthogonal to amplitude-based measures, including RMS and peak value, while exhibiting their strongest correlations with effective bandwidth ($r \approx 0.63$) and spectral entropy ($r \approx 0.49$). These observables quantify the redistribution and dispersion of energy across the time-frequency plane and serve as proxies for the coherence and complexity of elastic wave packets, independent of absolute signal scale or sensor modality.

This correlation structure indicates that \mathcal{F} responds

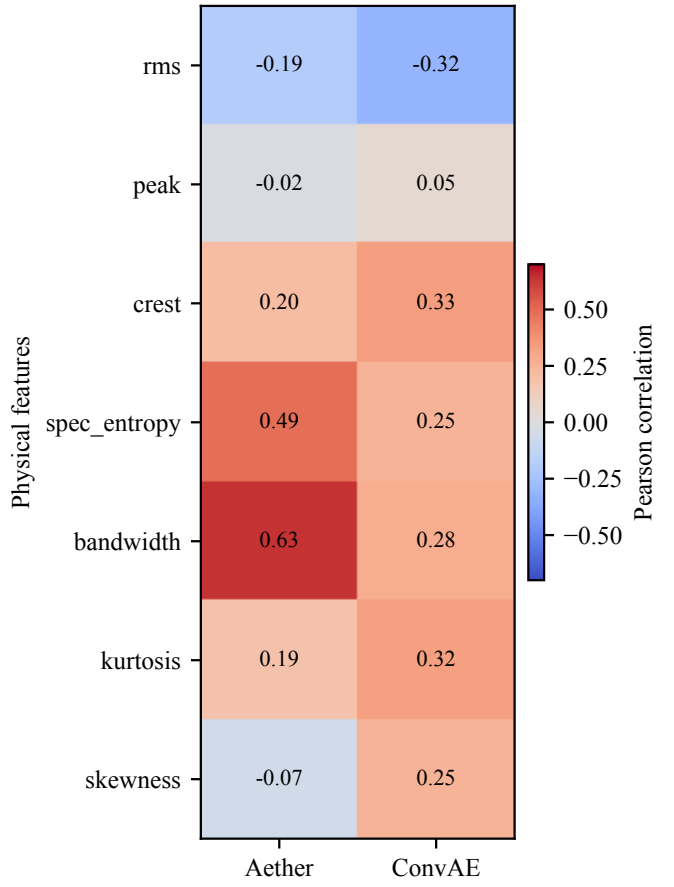


FIG. 5. Physical interpretability of anomaly scores. Pearson correlation between anomaly scores and classical signal descriptors. Reconstruction-based scores (ConvAE) exhibit stronger coupling to amplitude-related statistics, whereas the morphological operator \mathcal{F} correlates primarily with Effective Bandwidth and Spectral Entropy and remains largely orthogonal to signal energy.

preferentially to morphological decoherence—i.e., disruption of structured time-frequency organization—rather than to increases in signal power or variance. In physical terms, the operator is sensitive to *how* energy is organized across time and frequency, not to *how much* energy is present.

The contrasting correlation patterns of the ConvAE and \mathcal{F} therefore highlight a fundamental difference in the information encoded by the two approaches. Reconstruction-based methods remain implicitly tied to the energy and variance structure of the training data, while the latent operator \mathcal{F} isolates structural regularities associated with elastic wave propagation in constrained media. This decoupling from amplitude-driven detection provides a physically grounded interpretation of the selective zero-shot transfer observed in the preceding sections.

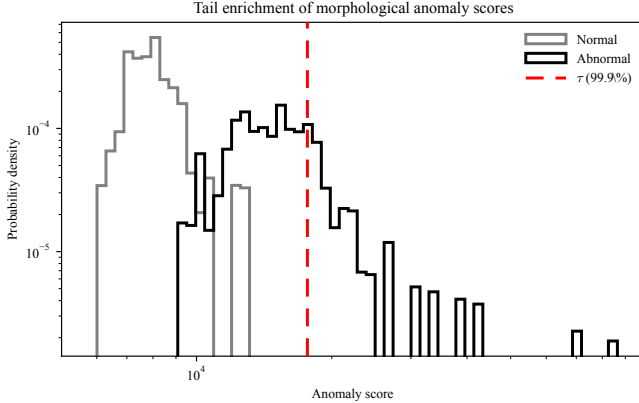


FIG. 6. Tail enrichment of morphological anomaly scores in the latent space. Log-scale probability density of window-level anomaly scores \mathcal{S} for nominal (gray) and fault-induced (black) mechanical states under the reverberation condition L_1 . The detection threshold τ is defined as the $q = 0.999$ quantile of the nominal distribution, corresponding to a nominal false-alarm rate of $1 - q = 10^{-3}$. Densities are estimated using logarithmically spaced histogram bins. Beyond this threshold, abnormal windows exhibit a pronounced excess of extreme events, with exceedance probability $\mathbb{P}(\mathcal{S} > \tau \mid \text{abnormal}) = 6.49 \times 10^{-2}$, yielding a tail enrichment factor $\Lambda_{\text{tail}} = 64.9$ (95% CI: [55.7, 74.5]). The separation is dominated by rare, high-score excursions rather than by shifts in central tendency.

G. Tail Enrichment of Extreme Morphological Events

Beyond aggregate discrimination metrics, we characterize anomaly sensitivity through the statistics of extreme events in the latent space. This analysis is deliberately aligned with rare-event detection paradigms in experimental physics, including gravitational-wave instrumentation, where physically meaningful signals are identified not by shifts in average behavior but by excess occupancy in the extreme tails of background distributions.

Rather than interpreting anomaly scores through their mean or variance, we analyze exceedance statistics relative to a fixed reference distribution constructed from nominal operation. Figure 6 shows the probability density of window-level anomaly scores \mathcal{S} under nominal and fault-induced mechanical conditions for the reverberation condition L_1 .

While the nominal anomaly-score distribution exhibits a rapidly decaying tail, fault-induced mechanical states display a pronounced excess of extreme latent events. At a fixed nominal false-alarm rate of 10^{-3} , defined by the $q = 0.999$ quantile of the nominal distribution, we observe a tail enrichment factor $\Lambda_{\text{tail}} = 64.9$, with a nonparametric bootstrap 95% confidence interval of [55.7, 74.5]. The observed nominal exceedance rate (1.01×10^{-3}) is consistent with the target false-alarm rate within finite-sample uncertainty.

Crucially, this separation is driven by rare, high-score excursions rather than by a global shift of the anomaly-score distribution. In physical terms, the latent operator \mathcal{F} responds to the emergence of transient windows exhibiting extreme morphological decoherence—i.e., strong disruption of structured time-frequency organization—analogous to excess-power or burst-like detection strategies in interferometric gravitational-wave searches.

Negative-control conditions, including electrically dominated signals and selected morphology-destruction transformations, do not exhibit tail occupancy above the nominal false-alarm rate. The absence of enrichment in these regimes confirms that the observed heavy-tail behavior is not a generic consequence of distributional mismatch, score rescaling, or non-Gaussianity per se, but arises specifically from preserved elastic transient morphology in mechanically governed systems.

We emphasize that Λ_{tail} is not interpreted as a discovery statistic and does not constitute a hypothesis test. Rather, it quantifies the degree to which fault-induced mechanical states populate the extreme-event regime of the latent space relative to nominal operation. As such, Λ_{tail} provides a physically grounded characterization of anomaly sensitivity consistent with the interpretation of \mathcal{F} as a morphological detector of rare, structured elastic transients.

IV. DISCUSSION

A. Resolution-Dependent Morphological Sensitivity and Conditional Invariance

The term “morphological invariance” is used here only as shorthand for a resolution-dependent stability of the operator response, not as a fundamental invariance of the underlying dynamics. It refers to the behavior of a fixed latent operator under changes of physical system, rather than to an invariance of the equations of motion. The observed behavior should therefore be interpreted as a representation-induced property of \mathcal{F} under a specific experimental protocol, not as evidence for a universal symmetry, conserved quantity, or scale-free law of elastic dynamics.

The scope of this work is deliberately restricted to systems governed by mechanically mediated elastic wave propagation in constrained solids. We do not attempt to optimize or validate the approach in regimes dominated by stochastic acoustic or electromagnetic processes.

The time-frequency resolution employed is chosen to resolve short-duration, broadband elastic transients while suppressing explicit dependence on absolute scale, sensor modality, and physical units through per-window normalization. At this resolution, elastic wave packets remain identifiable as structured objects in the time-frequency plane. Within this regime, anomaly sensitivity transfers across physically unrelated systems only when coherent

elastic transient morphology is preserved.

Crucially, this transfer occurs without retraining, fine-tuning, domain adaptation, or access to target-domain semantics. In the IMS and CWRU bearing experiments, the operator \mathcal{F} —trained exclusively on interferometric strain transients—exhibits monotonic drift detection, early time-to-detection, and pronounced tail enrichment under mechanical fault conditions, even when classical classification metrics such as window-level AUC vary substantially. This indicates that \mathcal{F} is not encoding system-specific operating conditions, but is responding to structural properties intrinsic to elastic wave propagation in constrained media.

B. Domain of Validity and Physical Selectivity

A central implication of these results is that the anomaly sensitivity exhibited by \mathcal{F} is not universal, but sharply conditional on the physical mechanisms governing signal generation and propagation. The systematic contrast observed between mechanically mediated systems and electrically dominated signals provides an explicit, experimentally grounded delineation of the domain in which the proposed approach is valid.

When applied to electrically dominated vibration signals, anomaly sensitivity collapses toward weak and non-selective behavior. Although window-level AUC values may remain marginally above chance, they lack the defining signatures observed in mechanically governed systems: stability under aggregation, monotonic temporal drift, and enrichment of extreme latent events. This collapse occurs despite the presence of non-Gaussian statistics, demonstrating that non-Gaussianity alone is insufficient to induce cross-domain anomaly sensitivity.

These observations indicate that \mathcal{F} does not respond to generic distributional shifts, broadband noise, or narrow-band electromagnetic interference. Instead, measurable sensitivity emerges only in systems that support mechanically mediated elastic wave propagation in constrained media. The absence of strong anomaly sensitivity in electrically dominated systems therefore functions as a negative control, reinforcing the physical selectivity of the operator rather than indicating a methodological limitation.

We do not claim that \mathcal{F} provides a first-principles representation of elastic dynamics. Rather, it functions as an empirical measurement instrument whose response reveals structural regularities when elastic wave propagation is coherent and constrained.

C. Physical Origin of Morphological Regularities

The conditional nature of the observed transfer admits a direct physical interpretation. Both interferometric instrumentation and rotating mechanical assemblies support elastic wave propagation in bounded, structured

media. In interferometers, transient disturbances excite elastic modes of suspended optical components and support structures; in rolling-element bearings, impacts and frictional contacts excite guided elastic waves in raceways, rolling elements, shafts, and housings.

The physical interpretation advanced here is operational: \mathcal{F} acts as a morphology-sensitive instrument under a specified preprocessing and scoring protocol, and its selectivity is established empirically through negative controls and controlled morphology-destruction interventions.

Recent work has shown that deep representations induce highly structured latent geometries reflecting both architecture and training data [15], while geometric deep learning highlights how inductive biases tied to data structure can dominate downstream behavior even under frozen, zero-shot deployment [16].

In both interferometric and mechanical systems, measured signals reflect the superposition, dispersion, and reflection of elastic wave packets constrained by geometry, material properties, and boundary conditions. These processes impose characteristic time-frequency organizations that are largely independent of absolute physical scale, yet highly sensitive to coherence and confinement. The empirical results indicate that \mathcal{F} is selectively sensitive to these regularities: when elastic propagation remains coherent, anomaly sensitivity, drift, and tail enrichment emerge; when this organization is disrupted, sensitivity degrades in a predictable, transformation-dependent manner.

D. Structural Sensitivity Beyond Energy-Based Detection

The comparative behavior between \mathcal{F} and reconstruction-based baselines admits a clear physical interpretation. Reconstruction-based anomaly detectors implicitly learn scale-dependent statistics of the training manifold, flagging deviations when test signals differ in amplitude, variance, or spectral power distribution. As a result, reconstruction error remains intrinsically coupled to energy-based cues.

In contrast, the latent operator \mathcal{F} encodes structural properties associated with elastic wave propagation in constrained media. Its anomaly sensitivity is governed not by absolute signal power, but by the organization of energy across time and frequency, reflecting the coherence and dispersion of propagating elastic wave packets. This decoupling from amplitude-driven cues explains why anomaly sensitivity can be preserved across domains with radically different sensing modalities, physical units, and energy scales.

The response of \mathcal{F} to controlled morphological degradation is therefore naturally interpreted as a loss of coherent time-frequency organization. Dispersion, temporal smearing, and reverberation progressively disrupt elastic transient structure, leading to a breakdown of the pat-

terns to which the latent representation is tuned.

E. Broader Physical Scope

Within its physically delimited domain of validity, the results suggest a broader implication: representations developed in precision physics contexts may encode structural priors that reflect general properties of wave-mediated dynamics in bounded media, rather than features tied to a specific instrument or dataset.

Under appropriate physical conditions, such representations can function as morphology-sensitive measurement devices rather than task-specific classifiers. The present results indicate that cross-domain transfer of anomaly sensitivity is physically mediated rather than algorithmic, and should therefore be expected only when underlying propagation mechanisms and morphological constraints are shared.

V. CONCLUSION

We have shown that anomaly sensitivity can transfer across physically unrelated systems when their measured signals preserve coherent elastic transient morphology. A latent operator trained exclusively on interferometric strain transients from gravitational-wave detector instrumentation exhibits robust zero-shot sensitivity when applied to rotating mechanical systems governed by elastic wave propagation, without retraining, fine-tuning, or domain adaptation.

The observed transfer is selective rather than generic. Pronounced anomaly sensitivity, monotonic drift, early time-to-detection, and enrichment of extreme latent events arise only in systems that support mechanically mediated elastic wave propagation in constrained media. In contrast, electrically dominated signals and controlled morphology-destruction transformations do not exhibit

these signatures, thereby defining a clear and physically motivated domain of validity. These negative results rule out explanations based on signal energy, marginal statistics, or generic distributional mismatch.

In run-to-failure regimes, the fixed operator yields a normalized and interpretable Health Index that tracks progressive degradation and identifies deviation from nominal operation well before catastrophic failure. This behavior persists even when classical classification metrics vary across runs, demonstrating sensitivity to structural evolution rather than to discrete fault labels.

These findings support an empirically observed, resolution-dependent morphological sensitivity, which can be described as a conditional invariance of the operator response under changes of physical system. Within the stated experimental protocol, the operator \mathcal{F} functions as a morphology-sensitive measurement device rather than as a task-specific classifier. More broadly, this work illustrates how representations developed for precision measurement in fundamental physics can encode transferable structural priors, enabling physically selective zero-shot generalization across systems that share common elastic propagation phenomenology.

DATA AND CODE AVAILABILITY

All raw target-domain sensor datasets used in this work are publicly available from their original providers (IMS–NASA, CWRU, and VSB) and are not redistributed here. Source-domain interferometric training data and trained model weights are not publicly released.

Figure-level computational reproducibility is provided through derived, non-invertible artifacts and deterministic scripts that regenerate all figures and numerical values reported in the manuscript. Full implementation, training, and preprocessing details are provided in the Supplemental Material.

Repository: <https://github.com/joseandreuu/aether-morphology-paper>

[1] J. Powell *et al.*, *Classical and Quantum Gravity* **32**, 215012 (2015).

[2] M. Zevin *et al.*, *Classical and Quantum Gravity* **34**, 064003 (2017).

[3] M. Cabero *et al.*, *Classical and Quantum Gravity* **36**, 155010 (2019).

[4] K. F. Graff, *Wave Motion in Elastic Solids* (Dover Publications, New York, 1975).

[5] B. A. Auld, *Acoustic Fields and Waves in Solids* (Wiley, New York, 1973).

[6] W. A. Smith and R. B. Randall, Rolling element bearing fault diagnosis data set, Case Western Reserve University Bearing Data Center (2015).

[7] P. D. McFadden and J. D. Smith, *Journal of Sound and Vibration* **96**, 69 (1984).

[8] W. A. Smith and R. B. Randall, *Mechanical Systems and Signal Processing* **64–65**, 100 (2015).

[9] R. B. Randall, *Vibration-based Condition Monitoring* (Wiley, 2011).

[10] Vsb power line fault detection dataset, <https://www.kaggle.com/c/vsb-power-line-fault-detection> (2019), electrically dominated high-voltage fault signals.

[11] V. Chandola, A. Banerjee, and V. Kumar, *ACM Computing Surveys* **41**, 15 (2009).

[12] L. Ruff *et al.*, in *Proceedings of the 35th International Conference on Machine Learning*, Proceedings of Machine Learning Research, Vol. 80 (2018) pp. 4393–4402.

[13] O. Ledoit and M. Wolf, *Journal of Multivariate Analysis* **88**, 365 (2004).

[14] H. Qiu, J. Lee, J. Lin, and G. Yu, Bearing data set, NASA Ames Prognostics Data Repository (2006), iMS run-to-failure bearing dataset.

- [15] R. Balestriero and R. Baraniuk, IEEE Transactions on Information Theory **67**, 5588 (2021).
- [16] M. M. Bronstein, J. Bruna, T. Cohen, and P. Velickovic, Nature Reviews Physics **3**, 752 (2021).